

## A conjugated heat and mass transfer model to implement reaction in particle-resolved CFD simulations of catalytic fixed bed reactors

Martin Kutscherauer, Scott D. Anderson, Sebastian Böcklein, Gerhard Mestl, Thomas Turek & Gregor D. Wehinger

**To cite this article:** Martin Kutscherauer, Scott D. Anderson, Sebastian Böcklein, Gerhard Mestl, Thomas Turek & Gregor D. Wehinger (2024) A conjugated heat and mass transfer model to implement reaction in particle-resolved CFD simulations of catalytic fixed bed reactors, *Engineering Applications of Computational Fluid Mechanics*, 18:1, 2292100, DOI: [10.1080/19942060.2023.2292100](https://doi.org/10.1080/19942060.2023.2292100)

**To link to this article:** <https://doi.org/10.1080/19942060.2023.2292100>



© 2024 The Author(s). Published by Informa UK Limited, trading as Taylor & Francis Group.



[View supplementary material](#)



Published online: 10 Jan 2024.



[Submit your article to this journal](#)



[View related articles](#)



[View Crossmark data](#)

# A conjugated heat and mass transfer model to implement reaction in particle-resolved CFD simulations of catalytic fixed bed reactors

Martin Kutscherauer<sup>a,b</sup>, Scott D. Anderson<sup>a</sup>, Sebastian Böcklein<sup>b</sup>, Gerhard Mestl<sup>b</sup>, Thomas Turek<sup>a</sup> and Gregor D. Wehinger<sup>a</sup>

<sup>a</sup>Institute of Chemical and Electrochemical Process Engineering, Clausthal University of Technology, Clausthal-Zellerfeld, Germany; <sup>b</sup>Clariant AG, Heufeld, Germany

## ABSTRACT

Modelling catalytic fixed bed reactors with a small tube-to-particle diameter ratio requires a detailed description of the interactions between fluid flow, intra-particle transport, and the chemical reaction(s) within the catalyst. Particle-resolved computational fluid dynamics (PRCFD) simulations are the most promising approach to predict the behaviour of these reactors accurately, since they take into account the local packed bed structure explicitly. In this work, a conjugated heat and mass transfer model for use in PRCFD simulations is presented in order to couple the fluid flow through the fixed bed with transport and reaction in the porous catalyst, while guaranteeing the no-slip boundary condition at the fluid–solid interface. For this purpose, the solutions of the solid and fluid domain are computed separately and are coupled by calculation and updating the boundary condition at the particle surface. Owing to the consideration of secondary gradients, the developed transfer model is also valid for unstructured calculation meshes containing non-orthogonal cells at the fluid–solid interface. Such meshes are often used to resolve complex geometries, such as a packed bed, in a computationally efficient manner. The coupling approach is validated using cases for which an analytical solution or literature correlations derived from experimental data are available. The simulation results of a short catalytic packed bed with rings catalysing the partial oxidation of *n*-butane to maleic anhydride exemplify the potential of PRCFD involving reactions to analyse the catalyst performance in great detail.

## ARTICLE HISTORY

Received 1 August 2023  
Accepted 3 October 2023

## KEYWORDS

Particle-resolved computational fluid dynamics; Conjugated heat and mass transfer; Heterogeneous catalysis; Catalytic fixed bed; Inter- and intra-particle transport

## 1. Introduction

Heterogeneously catalysed gas phase reactions are commonly carried out in fixed bed reactors throughout the chemical processing industry (Eigenberger & Ruppel, 2012). Slender tubes with only a few particles along the tube diameter are required for highly endothermic and exothermic reactions, such as the partial oxidation of *n*-butane to maleic anhydride (MA) (Müller et al., 2022), in order to supply or remove heat efficiently while keeping the pressure drop at a moderate level. Owing to the pronounced effect of the tube wall on the particle arrangement, the small tube-to-particle diameter-ratio ( $D_t/d_p < 10$ ) results in an inhomogeneous packed bed morphology (Ziółkowska & Ziółkowski, 1988), affecting fluid flow and heat and species mass transport (Dixon, 2021a), as well as chemical reactions (Wehinger et al., 2015). Since classical pseudo-continuum models are based on simplifying assumptions about the fixed bed geometry and the fluid flow, they cannot account for

effects caused by the local packed bed structure and may fail to describe such reactors accurately (Dixon, 2021b).

In contrast to classical continuum models, particle-resolved computational fluid dynamics (PRCFD) simulations can describe local phenomena, since the spatial domain is fully resolved and hence every single particle is taken into account when solving the governing equations for momentum, mass, energy and species mass (Dixon & Partopour, 2020). For the most part, the solution is computed numerically by discretizing the packed bed geometry with three-dimensional computational cells, i.e. the finite volume methods. In only a few studies, the lattice Boltzmann method is used, see e.g. Freund et al. (2003). The packed beds are typically generated synthetically, employing the discrete element method (Jurtz, Waldherr, et al., 2019) or the rigid body approach (Flaischlen & Wehinger, 2019). Most of the PRCFD studies available in the literature neglect chemical reactions to investigate the impact of the particle shape

**CONTACT** Gregor D. Wehinger  [wehinger@icvt.tu-clausthal.de](mailto:wehinger@icvt.tu-clausthal.de)  Institute of Chemical and Electrochemical Process Engineering, Clausthal University of Technology, Leibnizstr. 17, Clausthal-Zellerfeld38678, Germany

 Supplemental data for this article can be accessed online at <https://doi.org/10.1080/19942060.2023.2292100>.

© 2024 The Author(s). Published by Informa UK Limited, trading as Taylor & Francis Group.

This is an Open Access article distributed under the terms of the Creative Commons Attribution License (<http://creativecommons.org/licenses/by/4.0/>), which permits unrestricted use, distribution, and reproduction in any medium, provided the original work is properly cited. The terms on which this article has been published allow the posting of the Accepted Manuscript in a repository by the author(s) or with their consent.

(Dixon et al., 2005), the  $D_t/d_p$  ratio (Flaischlen et al., 2021) or inserts, such as heat fins (Jurtz et al., 2020) and thermowells (Kutscherauer et al., 2023) on pressure drop and heat transport. However, the strong interplay between transport phenomena and catalytic chemistry requires reactions to be implemented in PRCFD simulations in order to analyse a fixed bed reactor in a sufficiently high degree of detail.

If pore diffusion inside a catalyst particle is negligible (instantaneous diffusion), the reaction can be implemented as heat and species mass fluxes at the particle surface. Such an approach based on the operator splitting algorithm was proposed by Maestri and Cuoci (2013) to couple CFD with complex microkinetic reaction models. Since the active sites catalysing the gas-phase reaction are commonly located inside a porous structure solid and not directly on the particle surface, Wehinger et al. (2017) extended the method of Maestri and Cuoci (2013) by taking into account pore diffusion through an effectiveness factor calculated via the Thiele modulus. Nevertheless, the application of effectiveness factors cannot meet the requirements of an ideal multiscale model, as presented in Wehinger et al. (2022), since the impacts of intraparticle concentration gradients on the reaction are not precisely described. Therefore, Kolaczowski et al. (2007) suggested fully coupling transport and reaction inside the catalyst with the fluid flow by defining the particles as porous media. As pointed out by Dixon et al. (2010), the absence of a no-slip boundary condition at the particle surface, when using the porous media approach, results in an artificial convective transport into the solid domain. However, according to the physical and chemical steps in heterogeneous catalysis described in many textbooks, such as Ertl et al. (1997), species mass is only transported via diffusion inside the porous catalyst. To overcome this issue, Dixon et al. (2010) implemented user-defined scalars within the commercial CFD code Fluent<sup>®</sup> to model the diffusive species mass transport inside particles. The catalyst is assumed to be a pseudo-continuum. Moreover, the fluid flow is coupled with the solid region by iteratively calculating the boundary conditions for energy and species mass transport at the fluid–solid interface. Maffei et al. (2016) developed a similar method, capable of being employed in large microkinetic models, in the open-source CFD framework OpenFoam<sup>®</sup>.

The coupling approaches of Dixon et al. (2010) and Maffei et al. (2016) are able to describe the interaction between the surrounding fluid flow and reactions inside the porous catalyst correctly. However, they are only valid for computational meshes with orthogonal cells at the particle surface, since both methods neglect secondary gradients in the description of the heat and species mass transfer at the fluid–solid interface. For

computational efficiency, complex packed bed geometries are usually discretized with unstructured meshes (Kutscherauer et al., 2022) that often contain non-orthogonal cells at the particle surface. As pointed out by Demirdžić and Muzaferija (1995), the influence of the secondary gradient on the diffusion flux is small if the non-orthogonality is not severe. However, Pasdunkorale and Turner (2003) claimed that, for cases with a large change in transport parameters, accurate calculation of the secondary gradient becomes more important. The relevance of considering the gradient in PRCFD simulations of catalytic fixed beds is still an open question.

In this work, a conjugated heat transfer (CHT) and mass transfer (CMT) model is presented within the framework of PRCFD to couple the fluid flow with transport and reaction inside a porous catalyst, taking into account the secondary gradient. Owing to the analogy between heat and species mass transport, the definition of the CMT model is derived from the well established CHT model. Furthermore, the method presented is also valid for turbulent flows with  $y^+$  values of the wall-nearest cell being larger than one, because it applies wall functions to describe the heat and species mass transfer in turbulent flow regimes. This allows, in contrast to the aforementioned works of Dixon et al. (2010) and Maffei et al. (2016), coarser meshes to be used for the simulation of turbulent flows, which reduces the overall computational effort. This novel approach is validated using the analytical solution of heat and species mass diffusion through two connected slabs and standard literature correlations for the flow around a sphere. As an illustrative example, PRCFD simulations are presented for a short catalytic fixed bed containing ring shaped particles catalysing the selective oxidation of *n*-butane to maleic anhydride. In this industry relevant process,  $C_4H_{10}$  reacts with oxygen to MA over a vanadium phosphorus oxide (VPO) catalyst. As side reactions, *n*-butane as well as MA are oxidized to the unwanted by-products CO and  $CO_2$ . In addition, the water formed in the oxidation reaction inhibits the active sites of the catalyst and decreases its activity (Müller et al., 2021). In industry, this highly exothermic process is commonly carried out in multi-tubular fixed bed reactors with a small  $D_t/d_p$  ratio cooled by molten salt and fed with air as  $O_2$  source mixed with a mole fraction up to 2% of  $C_4H_{10}$ . The reactors are operated at a constant conversion of 80% to 86%, resulting in MA yields between 57% and 61% (Müller et al., 2022). Insufficient heat removal, particle overheating, and pore-diffusion limitation of MA lead to a reduced yield for higher conversion owing to the more favoured formation of CO and  $CO_2$ . Optimization of the catalyst design could partially solve these problems and would allow operation under more optimal conditions. A method for accurate

modelling of transport phenomena coupled with kinetics as shown in this work would be beneficial for such an optimization. For the catalytic fixed bed, the impact of the secondary gradients on the simulation results is investigated.

## 2. Governing equations

Fixed bed catalytic reactors, such as those used for the example reaction of *n*-butane to maleic anhydride chosen in this paper, are generally operated under steady-state. Nevertheless, the activity and selectivity of the catalyst changes dynamically during operation. However, since these changes occur on a much larger time scale compared to the reaction and transport phenomena, the system can be considered steady-state, if only one operating point is studied (Lesser et al., 2017). Therefore, steady-state governing equations are solved for the fluid and solid domain and coupled via the fluid–solid interface for energy and species mass transport.

### 2.1. Fluid domain

In the fluid domain, the conventional equations for conservation of total mass, momentum, energy, and species mass are solved. The detailed derivation and description of these equations can be found in many textbooks and publications, see e.g. Jurtz, Kraume, et al. (2019) and Jakobsen (2014).

Conservation of total mass:

$$\nabla \cdot (\rho_f \mathbf{u}) = 0 \quad (1)$$

Conservation of momentum:

$$\nabla \cdot (\rho_f \mathbf{u} \otimes \mathbf{u}) = -\nabla p + \nabla \cdot \mathbf{T} \quad (2)$$

with the viscous stress tensor  $\mathbf{T}$ :

$$\mathbf{T} = 2\mu_f \mathbf{D} - \frac{2}{3}\mu_f \nabla \cdot \mathbf{u} \mathbf{I} \quad (3)$$

with  $\mathbf{D}$  being the deformation tensor:

$$\mathbf{D} = \frac{1}{2} [\nabla \mathbf{u} + (\nabla \mathbf{u})^T] \quad (4)$$

Conservation of energy:

$$\begin{aligned} \nabla \cdot (\rho_f \mathbf{u} h_{\text{tot}}) &= \mathbf{u} \nabla p + (\mathbf{T} : \nabla \mathbf{u}) + \nabla \cdot (\lambda_f \nabla T) \\ &\quad - \nabla \cdot \sum_{i=1}^N \dot{\mathbf{m}}_i h_i \end{aligned} \quad (5)$$

with  $h_{\text{tot}}$  being the total mass specific enthalpy of the gas mixture and  $h_i$  being the partial mass specific enthalpy of

species *i*. The diffusive species mass flux  $\dot{\mathbf{m}}_i$  is calculated according to Fick's law.

Conservation of species mass:

$$\nabla \cdot (\rho_f \mathbf{u} w_i) = \nabla \cdot (\rho_f D_{m,i} \nabla w_i) \quad (6)$$

As suggested by Dixon et al. (2010), the conservation of one species mass *i* is implemented in terms of a user-defined passive scalar, which represents the mass fractions  $w_i$ . The molecular diffusion coefficient  $D_{m,i}$  of an individual component *i* in the mixture is computed with the approximation of Fairbanks and Wilke (1950) using binary diffusion coefficients determined via the semi-empirical correlation of Fuller et al. (1966). The calculation of molecular diffusion coefficients is described precisely in Section S1 of the online supplemental data for this article, which can be accessed at <https://doi.org/10.1080/0305215X.2023.2292100>. To guarantee the conservation of total mass, the equation of species mass conservation is solved for  $N-1$  species, and the  $N$ th species is determined by the definition that the mass fractions sum to unity:

$$w_N = 1 - \sum_{i=1}^{N-1} w_i \quad (7)$$

In every iteration step, the average molecular weight  $M_w$ , thermal conductivity  $\lambda_f$ , dynamic viscosity  $\mu_f$ , and specific heat capacity  $c_{p,f}$  of the multi-component fluid mixture are determined based on the calculated mass fractions  $w_i$  from the pure component values, which are assumed to be constant. Thereby,  $\lambda_f$ ,  $\mu_f$ , and  $c_{p,f}$  are computed by mass fraction weighted averaging of the pure component data, whereas  $M_w$  is determined by molar fraction weighted averaging of the component molecular weights  $M_{w,i}$ . All required pure component properties are given in Section S2 of the online supplemental data. In addition, the mixture density  $\rho_f$  is calculated with the ideal gas law:

$$\rho_f = \frac{p M_w}{\mathfrak{R} T} \quad (8)$$

The flow around particles is characterized by the dimensionless particle Reynolds number  $Re_p$ :

$$Re_p = \frac{u_{\text{in}} \rho_f d_p}{\mu_f} \quad (9)$$

with  $d_p$  being the diameter of a sphere with equal specific surface. According to Ziółkowska and Ziółkowski (1988), the flow starts to behave turbulently for  $Re_p > 300$ . The description of turbulent flow behaviour with the standard Navier–Stokes equations requires high mesh resolution and consequently results in an unfeasible computational effort for fixed beds. Therefore, the computationally efficient Reynolds-averaged Navier–Stokes

(RANS) approach is applied to model the turbulent transport (Shih et al., 1995). Thereby, the standard steady-state governing equations are formulated in terms of averaged solution variables and the stress tensor is modified by an additional tensor  $\mathbf{T}_{\text{RANS}}$ , which must be calculated by an appropriate turbulence model. Solving steady-state governing equations to simulate the transient characteristics of turbulence can lead to an inaccurate description of dynamic flow phenomena and convergence problems. However, this approach is commonly used in the PRCFD of catalytic fixed bed reactors since transient simulations of such complex geometries still demand unreasonable computational costs (Dixon & Partopour, 2020). In the work presented, the realizable  $k$ - $\epsilon$  turbulence model according to Shih et al. (1995) is chosen to compute  $\mathbf{T}_{\text{RANS}}$ . Moreover, the averaged diffusive heat and species mass flow in the bulk phase is calculated as a function of the turbulent eddy viscosity  $\mu_{\text{turb}}$  by changing the thermal conductivity to  $\lambda_f + (c_{p,f} \mu_{\text{turb}} / Pr_{\text{turb}})$  and the diffusion coefficient to  $D_{m,i} + (\mu_{\text{turb}} / Sc_{\text{turb}} \rho_f)$ .

## 2.2. Solid domain

Inside the porous catalyst particles, energy and mass are transported only via diffusion. Since it is computationally unfeasible to resolve the pore network of the catalyst in a particle-scale CFD simulation, the solid domain is modelled as a pseudo-continuum, for which energy and species mass transport are described in terms of effective transport parameters (Maffei et al., 2016). The reaction is implemented via volumetric energy and species source terms in the following steady-state conservation equations.

Conservation of energy:

$$-\nabla \cdot (\lambda_{\text{eff}} \nabla T) = \rho_s \sum_{j=1}^{N_{\text{react}}} \Delta H_{\text{react},j}^{\circ} r_j \quad (10)$$

with the molar reaction rate per catalyst mass  $r_j$ , the specific molar standard reaction enthalpy  $\Delta H_{\text{react},j}^{\circ}$  and the effective thermal conductivity  $\lambda_{\text{eff}}$  of the catalyst material.

Conservation of species mass:

$$-\nabla \cdot (\rho_{s,f} D_{\text{eff},i} \nabla w_i) = \rho_s M_{w,i} \sum_{j=1}^{N_{\text{react}}} v_{i,j} r_j \quad (11)$$

with the density of the gas mixture inside the solid  $\rho_{s,f}$  and the stoichiometric coefficient  $v_{i,j}$  of component  $i$  in reaction  $j$ . As described for the fluid domain, the species mass conservation equation is solved for  $N-1$  species and the  $N^{\text{th}}$  species results from total mass conservation. The effective diffusion coefficient  $D_{\text{eff},i}$  is calculated with

the approximation derived by Bosanquet (1944):

$$D_{\text{eff},i} = \left( \frac{1}{D_{m,i}} + \frac{1}{D_{\text{Kn},i}} \right)^{-1} \frac{\epsilon_{\text{cat}}}{\tau_{\text{cat}}} \quad (12)$$

with the catalyst porosity  $\epsilon_{\text{cat}}$ , the tortuosity  $\tau_{\text{cat}}$ , and the Knudsen diffusion coefficient  $D_{\text{Kn},i}$  describing the effect of the pore walls on the diffusion process:

$$D_{\text{Kn},i} = \frac{2}{3} r_{\text{cat}} \sqrt{\frac{8 \mathfrak{R} T}{M_{w,i} \pi}} \quad (13)$$

with the pore radius  $r_{\text{cat}}$  of the catalyst.

As an example of an industrially relevant heterogeneously catalysed reaction, the partial oxidation of  $n$ -butane to maleic anhydride over a vanadium phosphorus oxide catalyst is shown. The simplified reaction network of the highly exothermic process is given in Figure 1. The molar reaction rates of the five reactions are calculated with the rate equations derived from transport limitation free kinetic measurements by Müller et al. (2021). For the sake of clarity, the rate equations are listed in Section S4 of the online supplemental data. Moreover, the catalyst material properties are adapted from Müller et al. (2021):  $\lambda_{\text{eff}} = 0.585 \text{ W m}^{-1} \text{ K}^{-1}$ ,  $\epsilon_{\text{cat}} = 0.5$ ,  $\tau_{\text{cat}} = 3$ ,  $r_{\text{cat}} = 35 \text{ nm}$ ,  $\rho_s = 1620 \text{ kg m}^{-3}$ ,  $r_{\text{cat}} = 35 \text{ nm}$ ,  $\rho_s = 1620 \text{ kg m}^{-3}$ .

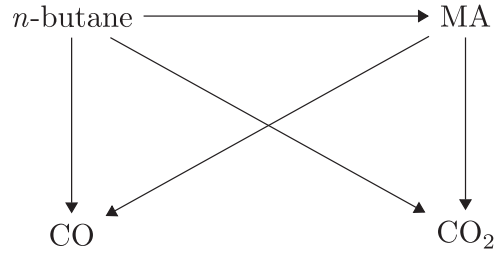
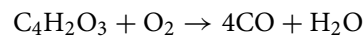
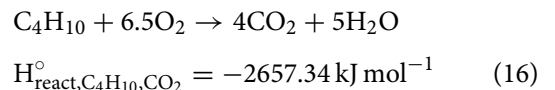
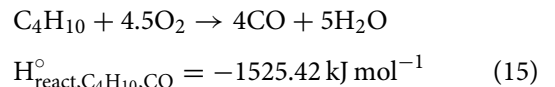
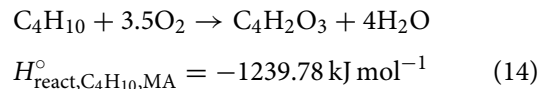
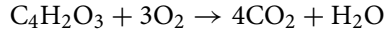


**Figure 1.** Reaction network for the partial oxidation of  $n$ -butane to maleic anhydride.

The stoichiometry of the reactions and their specific molar standard reaction enthalpy calculated from the standard formation enthalpy are defined by the following reaction equations:



$$H_{\text{react,MA,CO}}^{\circ} = -285.64 \text{ kJ mol}^{-1} \quad (17)$$



$$H_{\text{react,MA,CO}_2}^{\circ} = -1417.56 \text{ kJ mol}^{-1} \quad (18)$$

Besides the reactants and products  $\text{C}_4\text{H}_{10}$ ,  $\text{O}_2$ , MA, CO,  $\text{CO}_2$ , and  $\text{H}_2\text{O}$ , also  $\text{N}_2$  is considered as inert species in the gas mixture, since air provides the oxygen consumed by the oxidation reactions. Furthermore, oxygen is chosen as the  $N^{\text{th}}$  species and results from the total mass conservation, since it takes part in the reaction and is present in excess (Kee et al., 1986).

### 2.3. Fluid–solid interface

Since energy and mass are exclusively transferred by diffusion across the fluid–solid interface, a no-slip boundary condition for the fluid flow is applied at the particle surface to prevent artificial convective transport into the particle (Dixon et al., 2010). The implemented conjugated heat and mass transfer model couples the diffusive boundary fluxes of heat and species mass between the fluid and solid domains of the interface. Owing to the analogy of heat and mass transport, heat and species mass diffusion can generally be described as a diffusive flux  $\dot{\omega}$  of a scalar  $\phi$ .

#### 2.3.1. Description of boundary fluxes

The boundary flux in the direction of the boundary face normal is calculated by values stored in the centroid of the boundary-nearest mesh cell (subscript c) and in the face centroid of the boundary (subscript b). For a laminar flow and in the solid domain, the scalar boundary flux  $\dot{\omega}_b$  can be determined according to Murthy and Mathur (1998) with

$$\dot{\omega}_b = \kappa (\phi_b - \phi_c) + \dot{S}_\kappa \quad (19)$$

As visualized in Figure 2,  $\phi_c$  and  $\phi_b$  are the scalar values at the cell and boundary face centroid. The transfer coefficient  $\kappa$  is calculated with the gas mixture dependent

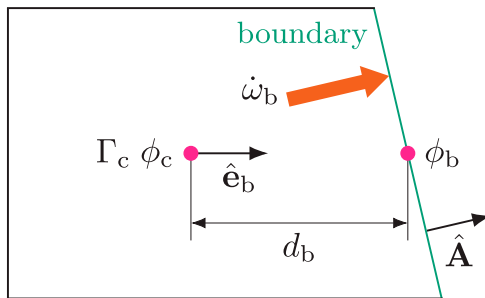


**Figure 2.** Schematic of the boundary adjacent cell and notation for the calculation of the boundary flux.

transport parameter  $\Gamma_c$  by reordering Fourier's and Fick's law, respectively:

$$\kappa = \frac{\hat{\mathbf{A}} \cdot \hat{\mathbf{A}}}{\hat{\mathbf{A}} \cdot \hat{\mathbf{e}}_b} \frac{\Gamma_c}{d_b} \quad (20)$$

with the boundary face normal  $\hat{\mathbf{A}}$ , the length  $d_b$  of the vector between the cell centroid and the boundary face centroid, and its normalization  $\hat{\mathbf{e}}_b$ .

Evaluating the difference of the scalar stored in the cell and face centroid not along the direction of the boundary face normal results in an additional flux aligned tangentially to the boundary face. The secondary gradient or cross diffusion term  $\dot{S}_\kappa$  describes the impact of this tangential flux on the boundary flux  $\dot{\omega}_b$  orientated in the direction of  $\hat{\mathbf{A}}$ . The method of Mathur and Murthy (1997) is applied to compute  $\dot{S}_\kappa$  explicitly:

$$\dot{S}_\kappa = \Gamma_c \left( \nabla \phi_c \cdot \hat{\mathbf{A}} - \nabla \phi_c \cdot \hat{\mathbf{e}}_b \frac{\hat{\mathbf{A}} \cdot \hat{\mathbf{A}}}{\hat{\mathbf{A}} \cdot \hat{\mathbf{e}}_b} \right) \quad (21)$$

For an orthogonal computational cell,  $\hat{\mathbf{A}}$  and  $\hat{\mathbf{e}}_b$  are equal resulting in  $\hat{\mathbf{A}} \cdot \hat{\mathbf{A}} / \hat{\mathbf{A}} \cdot \hat{\mathbf{e}}_b = 1$ , so that  $\dot{S}_\kappa$  is zero and can be neglected as suggested by Dixon et al. (2010). However, in a non-orthogonal computational cell,  $\hat{\mathbf{A}}$  can differ from  $\hat{\mathbf{e}}_b$  and the secondary gradient must be considered in the calculation of the boundary fluxes.

In a turbulent flow regime modelled with the RANS approach, the impact of turbulence on the boundary fluxes cannot be resolved by the mesh. Therefore, the transfer of the scalar from the cell centroid to the boundary face centroid is described by Newton's law leading to a formulation of the boundary flux identical with that given in Equation (19) for laminar flow, but without the secondary gradient. In contrast to the laminar case, the transfer parameter  $\kappa$  depends not only on the transport parameters  $\Gamma_c$  and the geometry of the computational cell, but also on the local flow regime. The transfer parameter is computed as a function of the velocity scale  $u^*$  and the dimensionless scalar  $\phi^+$ . These values are calculated with the blended wall function for velocity according to Reichardt (1951) and for scalar transport suggested by Kader (1981). The applied wall functions are comprehensively presented in Section S3 of the online supplemental data.

Table 1 summarizes the physical quantities used in the calculation of boundary heat and species mass fluxes according to the general formulations of the scalar boundary flux described.

#### 2.3.2. Description of fluxes and scalar values at the fluid–solid interface

At the fluid–solid interface, both domains share one boundary face. The values of the boundary fluxes and the

**Table 1.** Physical quantities for the computation of boundary heat and species mass fluxes.

Quantity	Heat flux	Species mass flux
$\phi$	$T$	$w_j$
$\Gamma_c$	$\lambda_c$	$\rho_c D_{i,c}$
$\kappa_{\text{lam/s}}$		$\frac{\hat{\mathbf{A}} \cdot \hat{\mathbf{A}}}{\hat{\mathbf{A}} \cdot \hat{\mathbf{e}}_b} \frac{\Gamma_c}{\partial_b}$
$\dot{S}_\kappa$		$\Gamma_c (\nabla \phi_c \cdot \hat{\mathbf{A}} - \nabla \phi_c \cdot \hat{\mathbf{e}}_b \frac{\hat{\mathbf{A}} \cdot \hat{\mathbf{A}}}{\hat{\mathbf{A}} \cdot \hat{\mathbf{e}}_b})$
$\kappa_{\text{turb}}$	$c_{p,c} \frac{\rho_c u^*}{T^+}$	$\frac{\rho_b u^*}{w_j^+}$

scalar values at the fluid and solid domains of the shared boundary face must be equal:

$$\begin{aligned} \dot{\omega}_{b,s} &= -\dot{\omega}_{b,f} \\ \phi_{b,s} &= \phi_{b,f} \end{aligned} \quad (22)$$

Combining these physical conditions with the formulation of the boundary flux in Equation (19) enables the calculation of the flux  $\dot{\omega}_{f,s}$  and the scalar value  $\phi_{f,s}$  at the fluid–solid interface based only on values stored in the interface-nearest cell centroid of the fluid and solid side (Murthy & Mathur, 1998):

$$\dot{\omega}_{f,s} = \frac{\kappa_s \kappa_f}{\kappa_s + \kappa_f} (\phi_{c,s} - \phi_{c,f}) - \frac{\dot{S}_{\kappa,s} \kappa_f - \dot{S}_{\kappa,f} \kappa_s}{\kappa_s + \kappa_f} \quad (23)$$

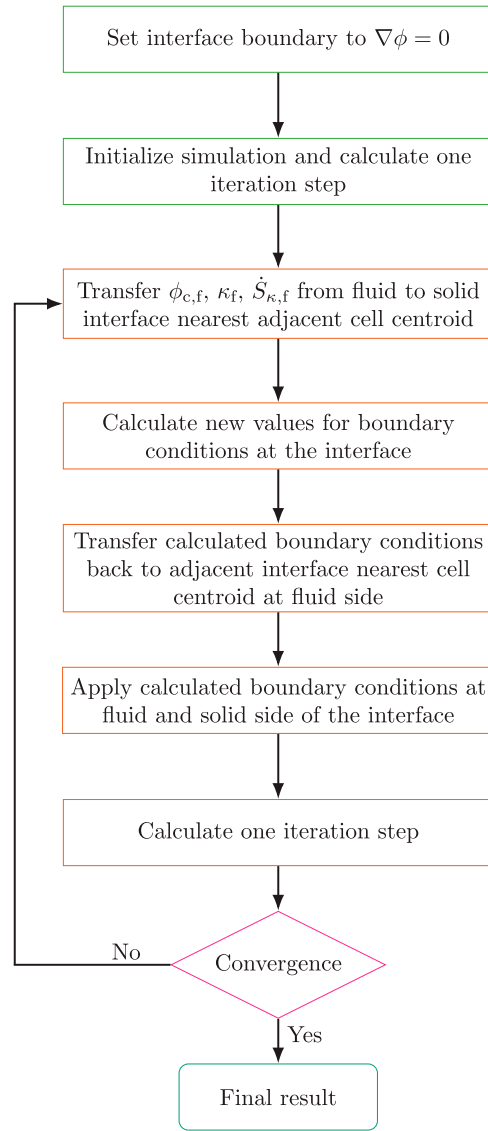
$$\phi_{f,s} = \frac{\phi_{c,s} \kappa_s + \phi_{c,f} \kappa_f}{\kappa_s + \kappa_f} - \frac{\dot{S}_{\kappa,s} + \dot{S}_{\kappa,f}}{\kappa_s + \kappa_f} \quad (24)$$

with  $\dot{S}_{\kappa,f} = 0$  for a turbulent fluid flow.

The derived equations of  $\dot{\omega}_{f,s}$  and  $\phi_{f,s}$  are only valid for a mesh in which a face at the interface is shared by one cell at the fluid side and one cell at the solid side. This type of mesh at the interface between two domains is called conformal.

### 3. Numerical methodology

As suggested by Maffei et al. (2016), a partitioned approach is applied to solve the governing equations of the coupled domains. Therefore, the solutions for the fluid and solid phases are computed iteratively in parallel but separated from each other by the segregated solver employing the SIMPLE algorithm within the commercial software Siemens Simcenter STAR-CCM+ 2021.1. The domains are coupled via calculation and updating of the boundary conditions at the shared fluid–solid interface during the iteration procedure. Figure 3 summarizes the calculation steps executed over a Java code within an iteration loop. The data mapper functionality of STAR-CCM+ is applied to transfer  $\phi_{c,f}$ ,  $\kappa_f$ , and  $\dot{S}_{\kappa,f}$  stored in the interface-nearest cell centroid at the fluid side to the adjacent interface-nearest cell centroid of the solid side. The values of the flux  $\dot{\omega}_{f,s}$  or scalar  $\phi_{f,s}$  at the interface are computed with the transferred quantities from

**Figure 3.** Flow chart of the iteration procedure.

the fluid side and the corresponding variables  $\phi_{c,s}$ ,  $\kappa_s$ , and  $\dot{S}_{\kappa,s}$  of the solid side according to Equations (23) or (24). The determined boundary condition is transferred back to the cell centroid of the fluid side and is applied as Neumann ( $\dot{\omega}_{b,s} = -\dot{\omega}_{b,f} = \dot{\omega}_{f,s}$ ) or Dirichlet ( $\phi_{b,s} = \phi_{b,f} = \phi_{f,s}$ ) boundary conditions at both sides of the interface. Finally, the next iteration step to solve the governing equation at both domains is performed and the loop starts over. After each step, convergence is checked by monitoring residuals and the closure of the species mass and energy balance at the fluid–solid interface and over the entire domains. The iteration loop stops if convergence is reached.

In general, it makes no difference what type of boundary condition is used at the fluid–solid interface. However, in STAR-CCM+ only the Dirichlet boundary in species mass transport and the Neumann boundary in

heat transport considers the secondary gradient. Hence, for heat transport the heat flux, and for species mass transport the mass fraction, are applied as boundary conditions at the interface. Moreover, STAR-CCM+ provides the option to neglect secondary gradients in the definition of boundary conditions. Doing so, the value of  $\hat{S}_{\kappa,f}$  and  $\hat{S}_{\kappa,s}$  must be set to zero for the calculation of the flux and scalar at the interface.

Owing to the rapid change in the calculated boundary condition at the interface, updating the boundary scalar or flux with every iteration results in divergence of the simulation. This is illustrated by the example shown in Figure 4 (top) for flow past a sphere, as described in Section 4.2, with a constant heat source inside the sphere (orange line). Decreasing the update frequency to 10 iterations until update (IUU) yields in a converged solution (the magenta line). However, reducing the update frequency increases the number of iteration steps until convergence is reached and consequently the overall computational time of the simulation. Therefore, an under-relaxation factor  $\tau$  is introduced, which is used to determine the new boundary condition  $\zeta$  by mixing the calculated boundary value  $\zeta_i$  with the currently applied one  $\zeta_{i-1}$  in the ratio given by  $\tau$ :

$$\zeta = \tau \zeta_i + (1 - \tau) \zeta_{i-1} \quad (25)$$

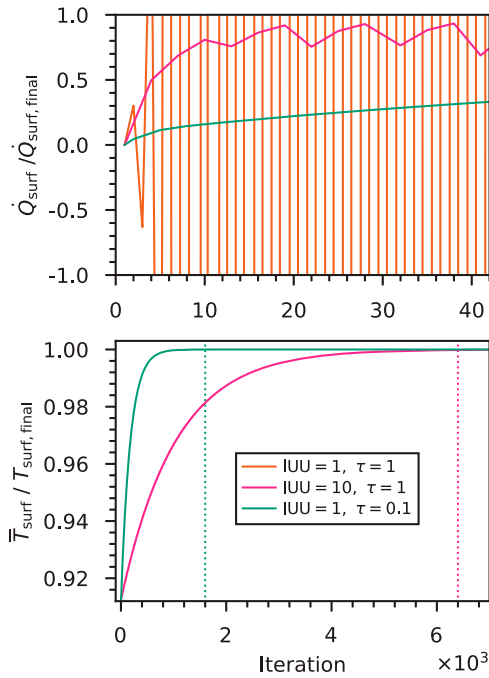


**Figure 4.** Convergence behaviour of the conjugated heat transfer model for flow past a sphere with a constant volumetric heat source inside the sphere applying various update frequencies (IUU: iterations until update) and under-relaxation factors  $\tau$  (at  $Re_p = 200$ ,  $\dot{S} = 4 \text{ W m}^{-3}$ ).

The application of an under-relaxation factor  $\tau = 0.1$  results in four times faster convergence than decreasing the update frequency, as shown in Figure 4 (bottom) by the green line.

If the angle between the boundary face normal  $\hat{\mathbf{A}}$  and the normalized vector from the cell centroid to the boundary face centroid  $\hat{\mathbf{e}}_b$  (the skewness angle) is larger than  $90^\circ$ , the transfer coefficient  $\kappa$  takes on negative values resulting in numerical problems and a non-physical solution. Therefore, the skewness angle is limited to  $88^\circ$ , corresponding to  $\hat{\mathbf{A}} \cdot \hat{\mathbf{e}}_b = 0.035$ , in the implemented calculation routine of the transfer coefficients. This enables simulations based on computational meshes containing boundary cells with skewness angle close to  $90^\circ$  or larger. Nevertheless, for an accurate solution, it is recommended that skewness angles larger than  $88^\circ$  be prevented in the applied mesh. All meshes used in the present study follow this recommendation.

#### 4. Simulation setup

The implemented conjugated heat and mass transfer model for coupling the reaction inside the porous catalyst with the fluid flow is tested and validated for three different geometries as illustrated in Figure 5. A visualization of the meshes utilized for these geometries can be found in Section S5.1 of the online supplemental data. All simulations are performed on a 64 bit server with two AMD Epyc 7281 processors (32 CPUs in total) and 512 GB RAM.

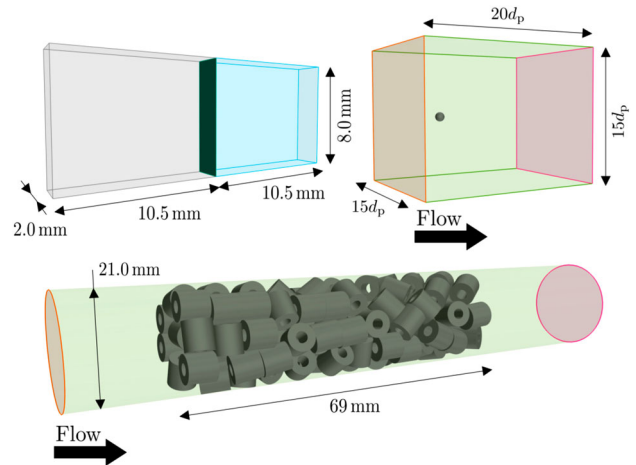


**Figure 5.** Investigated geometries: two connected slabs (top left) with an interface (dark green) between the solid (grey) and fluid (blue) domains; sphere in a rectangular channel (top right) with spherical VPO catalyst particle (grey), confining wall (green), inlet (orange) and outlet (red); tube containing short catalytic fixed bed (bottom) with ring shaped VPO catalyst particles (grey), confining wall (green), inlet (orange) and outlet (red).

#### 4.1. Heat and species mass diffusion through two connected slabs

Two slabs representing the fluid and solid domains are connected via an interface (see Figure 5, top left). The dimensions of both slabs are identical and set to 8.0 mm × 2.0 mm × 10.5 mm (Height × Width × Length). Energy and the two model species A and B are only transported via diffusion. Dirichlet boundary conditions for the temperature ( $T_{\text{surf},s} = 500$  K,  $T_{\text{surf},f} = 350$  K) and the mass fractions ( $w_{\text{surf},s,A} = 0.00$ ,  $w_{\text{surf},f,A} = 0.01$ ) are applied at the opposing surfaces of the two slabs. The remaining walls are set as adiabatic and impermeable, respectively. The thermal conductivity and the diffusion coefficients differ between the solid ( $\lambda_s = 0.6$  W m<sup>-1</sup> K<sup>-1</sup>,  $D_{s,A,B} = 5 \times 10^{-6}$  m<sup>2</sup> s<sup>-1</sup>) and the fluid ( $\lambda_f = 0.3$  W m<sup>-1</sup> K<sup>-1</sup>,  $D_{f,A,B} = 10 \times 10^{-6}$  m<sup>2</sup> s<sup>-1</sup>) phase, but are constant within the respective domains. Moreover, the density is considered as invariant and chemical reaction is excluded, so that the simulation can be compared with the analytical solution of the problem described in Section S6 of the online supplemental data. A structured mesh (total cell count:  $4.28 \times 10^4$ ) containing only orthogonal cells and an unstructured mesh (total cell count:  $2.66 \times 10^4$ ) with polyhedral cells is used for the numerical calculation.

#### 4.2. Flow around a spherical VPO catalyst particle

The flow around a single spherical VPO particle ( $d_p = 5$  mm) in a rectangular channel (see Figure 5, top right) coupled with reaction inside the catalyst is calculated for particle Reynolds numbers ranging from 50 to 1500. According the findings of Dixon et al. (2011), the sphere is placed  $5d_p$  from the inlet and the size of the box is chosen to be  $15d_p \times 15d_p \times 20d_p$  (Height × Width × Length) to guarantee a solution being independent of the domain size.

A polyhedral mesh is applied with a base cell size of  $d_p/10$  and a refinement of  $d_p/20$  in the wake and  $d_p/100$  at the particle surface. Layers of prismatic cells are created at both sides of the particle surface as suggested by Dixon et al. (2010). According to Dhole et al. (2006), the total thickness of the prism layers in the fluid domain are set to the thickness of the momentum boundary layer  $\delta_m$  in the stagnation point of a sphere at the highest investigated  $Re_p$ , which was derived by Schlichting and Gersten (2017).

$$\frac{\delta_m}{d_p} = 1.13 Re_p^{-0.5} \quad (26)$$

The prism layer thickness in the solid domain is set to 0.2 mm. Ten prism layers with a stretching factor of 1.1

are used at the fluid side and five prism layers within the particle stretched by a factor of 1.5. The generated mesh consists of 2.2 million cells in the fluid and 0.4 million cells in the solid domain. To ensure a solution independent of the mesh size, a mesh dependency study is carried out, which is presented in Section S5.2 of the online supplemental data.

The inlet velocity is uniformly distributed and defined according the investigated  $Re_p$ . At the outlet, a constant pressure of 101.325 kPa is specified and symmetry boundary conditions are applied for the confining walls. The composition and temperature of the entering fluid are similar to the conditions in the hot spot region of an industrial reactor for MA production reported by Lesser et al. (2016) ( $T_{\text{in}} = 730$  K,  $x_{\text{CO}} = 0.25\%$ ,  $x_{\text{CO}_2} = 0.20\%$ ,  $x_{\text{C}_4\text{H}_{10}} = 1.30\%$ ,  $x_{\text{H}_2\text{O}} = 2.00\%$ ,  $x_{\text{MA}} = 0.30\%$ ,  $x_{\text{O}_2} = 18.5\%$ ,  $x_{\text{N}_2} = 77.45\%$ ).

#### 4.3. Flow through a short catalytic fixed bed with VPO catalyst rings

The conjugated heat and mass transfer model presented is applied to flow and chemical reaction in a wall cooled tube ( $D_t = 21$  mm) filled with ring shaped VPO catalyst particles ( $d_{p,\text{outer}}/h_p/d_{p,\text{inner}} = 1/1/0.4$ ,  $D_t/d_{p,\text{outer}} = 3.75$ ). As characteristic size  $d_p$  of the ring, the diameter of a sphere with identical specific surface is used.

The fixed bed (see Figure 5, bottom) is synthetically generated with the rigid body approach implemented in the open source game engine Blender 2.79 (Flaischlen & Wehinger, 2019). The employed filling algorithm based on the work of Partopour and Dixon (2017) generates individual particles above the tube with randomized position and orientation. The particles fall down owing to gravity and fill up the tube. The algorithm stops generating new rings after 100 particles have been dropped, which results in a packed bed length of  $L_t = 69$  mm.

The mesh with polyhedral cells is generated according to the routine described in Kutscherauer et al. (2022). To ensure a high quality mesh, particle–particle and particle–wall contacts are locally replaced by a defined gap of size  $0.8\%d_{p,\text{outer}}$  containing fluid cells, i.e. a modified local caps method. The base size, which is a characteristic dimension for the cell size in Simcenter STAR-CCM+, is set to 7 mm. The size of the mesh on the particle surface is defined as 5% of the base size. At the outer particle surface and the tube wall, three prism layers are generated with a total thickness equal to the size of the momentum boundary layer calculated according to Equation (26). In addition, three layers of prismatic cells with a total thickness of 0.2 mm are introduced on the solid side of the particle surface. For close proximity surfaces, the surface mesh is refined and the number of prismatic cells is reduced

or completely rejected to reach a higher mesh quality. The cell count of the resulting mesh is 3.1 million for the fluid and 2.5 million for the solid phases. Kutscherauer et al. (2022) demonstrated by a mesh dependency study that the mesh size and settings used provide a physically accurate solution in a reasonable computational time for the applied particle and tube dimensions.

The uniformly distributed inlet velocity is specified to achieve a particle Reynolds number of 200. The outlet pressure is set to 101.325 kPa. The tube wall is impermeable to the species mass transport. Furthermore, at the tube wall, a no-slip boundary for the flow and a constant temperature  $T_{\text{wall}}$  are imposed as boundary conditions. The composition of the entering fluid and the temperatures at the inlet and wall are comparable to the conditions in the inlet region of an industrial scale MA reactor ( $T_{\text{in}} = T_{\text{wall}} = 673$  K,  $x_{\text{CO}} = x_{\text{CO}_2} = 0.00\%$ ,  $x_{\text{C}_4\text{H}_{10}} = 1.50\%$ ,  $x_{\text{H}_2\text{O}} = 1.80\%$ ,  $x_{\text{O}_2} = 21.00\%$ ,  $x_{\text{N}_2} = 75.70\%$ ).

## 5. Results

### 5.1. Two slabs: validation with analytic solution

The analytical solution to the boundary value problem described in Section 4.1 consists of linear profiles for the temperature and mass fractions of species A and B. Owing to the varying thermal conductivity  $\lambda$  and diffusion coefficient  $D_{A,B}$  of the solid and fluid phases, the slope of the profiles in the two domains is different resulting in a kink at the fluid–solid interface. Independent of whether the underlying mesh is structured or unstructured, the temperature and mass fraction profiles numerically calculated by applying the conjugated heat and mass transfer model at the fluid–solid interface

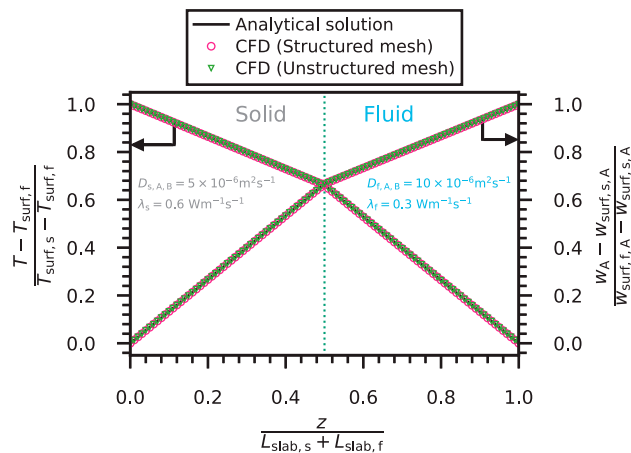


**Figure 6.** CFD with the conjugated heat and mass transfer model versus the analytic solution for heat and species mass diffusion through two connected slabs with different transport parameters.

agree excellently with the analytical solution, as shown in Figure 6. The deviation of the numerical from the analytical solution for the mass fraction of component A at the interface is  $5.0 \times 10^{-5}\%$  with a structured and  $3.9 \times 10^{-4}\%$  with an unstructured mesh, respectively. For the temperature at the interface, the numerical solution differs by  $6.0 \times 10^{-9}\%$  with the structured and by  $1.3 \times 10^{-4}\%$  with the unstructured mesh from the analytical solution. The higher deviation of the simulation based on an unstructured mesh can be attributed to the increase of numerical diffusion when polyhedral computational cells, which are not aligned in the direction of the diffusive flux, are used instead of orthogonal computational cells. Nevertheless, the numerical results are sufficiently accurate, no matter which mesh type is applied.

### 5.2. Flow past a sphere: comparison with correlations

The computed axial velocity, temperature, and mass fraction profiles along a line through the forward stagnation point for flow around a spherical VPO particle coupled with reaction inside the porous catalyst, as described in Section 4.2, are shown as an example for  $Re_p = 1500$  in Figure 7. Owing to the no-slip boundary condition at the fluid–solid interface, the velocity approaches zero at the particle surface and artificial convective heat and species mass fluxes as in the porous media approach proposed by Kolaczowski et al. (2007) are prevented. Owing to

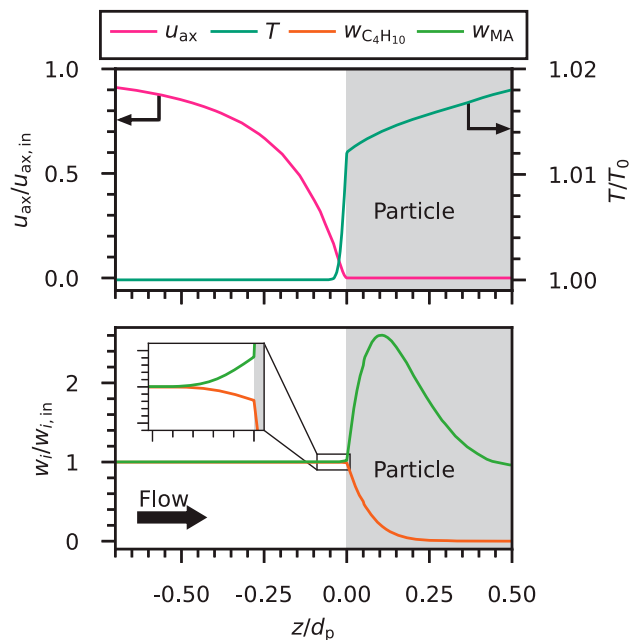


**Figure 7.** Axial velocity, temperature, maleic anhydride, and *n*-butane mass fraction profiles along a line through the stagnation point for flow past a sphere ( $Re_p = 1500$ ).

the exothermic reaction, the temperature increases inside the catalyst and near the particle surface. The temperature gradient is steeper at the fluid side of the interface than inside the particle, indicating that heat transport is limited by the heat transfer between fluid bulk and particle surface. In contrast, the limitation of species mass transport is larger inside the particle than at the fluid–solid interface, owing to the influence of Knudsen diffusion on the intra-particle transport. This leads to steep gradients of mass fractions inside the particle and flat concentration profiles at the fluid side of the particle surface. The reactions occurring consume *n*-butane and consequently the fraction of  $C_4H_{10}$  decreases inside the catalyst. Within the near-surface region of the particle ( $0.0 < z/d_p < 0.1$ ), the formation of maleic anhydride is the dominant reaction and  $w_{MA}$  increases. Since the transport of MA into the fluid phase is limited by pore diffusion, the maleic anhydride formed is partially further oxidized to CO and  $CO_2$  in the inner region of the catalyst resulting in a reduction of  $w_{MA}$  towards the particle centre.

The validity of applying the implemented conjugated heat and mass transfer model for coupling fluid flow with reaction within a porous catalyst is verified by the integral energy and material balances of the simulation. Therefore, the flow of energy and *n*-butane within the particle and at the fluid and solid sides of the interface are calculated by integrating the source terms over the catalyst volume and the diffusive fluxes over the particle surface. Moreover, the overall change of energy and *n*-butane in the fluid phase is determined by mass-weighted integration of the fluxes over the inlet and outlet sections of the fluid domain. Table 2 lists the computed values for the laminar ( $Re_p = 200$ ) and turbulent ( $Re_p = 1500$ ) cases. Owing to conservation of energy and species mass, the amount of all four computed values must be equal.

For the laminar flow, the deviation from the integrated particle source terms ranges between  $1.48 \times 10^{-8}\%$  and  $3.20 \times 10^{-3}\%$ . The highest error can be found for the change in the species mass flow of  $C_4H_{10}$  between inlet and outlet, which can be attributed to a small inaccuracy in the overall mass balance as already reported by Dixon et al. (2010). In the turbulent case, the error in the

heat and species mass balance is between  $6.34 \times 10^{-5}\%$  and  $1.78 \times 10^{-2}\%$ . The maximum deviation from the integrated particle source terms is located on the fluid side of the interface, owing to the oscillating convergence behaviour of the  $k-\epsilon$  turbulence model in the region of the highest wall share stress ( $20^\circ$  to  $80^\circ$  from the forward stagnation point). This can be attributed to unsteady flow phenomena occurring in the investigated high subcritical particle Reynolds number range (Clift et al., 2013). However, the small errors in the energy and material balance are in an acceptable range and demonstrate that the CHT and CMT model is able to couple flow and reaction between a porous catalyst and the surrounding flow field correctly.

Besides checking overall energy and species mass conservation, the particle Nusselt number  $Nu_p$  and the particle Sherwood number of *n*-butane  $Sh_{p,C_4H_{10}}$  are determined from the CFD simulation of flow around a spherical VPO catalyst particle and compared with literature correlations for different  $Re_p$  numbers:

$$Nu_p = \frac{h d_p}{\lambda_f} \quad (27)$$

$$Sh_{p,C_4H_{10}} = \frac{k_{C_4H_{10}} d_p}{D_{m,C_4H_{10}}} \quad (28)$$

The overall heat transfer  $h$  and mass transfer  $k_{C_4H_{10}}$  coefficients are determined by

$$h = \frac{\dot{Q}_s}{A_p (T_{surf} - T_{in})} \quad (29)$$

and

$$k_{C_4H_{10}} = \frac{\dot{M}_{s,C_4H_{10}}}{A_p (w_{surf,C_4H_{10}} - w_{in,C_4H_{10}})} \quad (30)$$

where  $\dot{Q}_s$  and  $\dot{M}_{s,C_4H_{10}}$  are calculated by integrating the heat and  $C_4H_{10}$  source terms of the CFD simulation over the particle volume. The surface temperature  $T_{surf}$  and mass fraction  $w_{surf,C_4H_{10}}$  are evaluated by area averaging temperatures and mass fractions from the CFD simulation over the particle surface. Figure 8 shows that heat and species mass transfer from the particle surface into the fluid phase grows with increasing  $Re_p$ . The  $Nu_p$  and

**Table 2.** Heat and  $C_4H_{10}$  species mass flow integrated over the particle volume, the fluid and solid side of the interface and between domain inlet and outlet as well as their relative deviation from the integrated particle source terms for flow past a sphere.

	Laminar ( $Re_p = 200$ )				Turbulent ( $Re_p = 1500$ )			
	$\dot{Q}$ (W)	Deviation (%)	$\dot{M}_{C_4H_{10}}$ ( $kg\ s^{-1} \times 10^{-9}$ )	Deviation (%)	$\dot{Q}$ (W)	Deviation (%)	$\dot{M}_{C_4H_{10}}$ ( $kg\ s^{-1} \times 10^{-9}$ )	Deviation (%)
Particle	0.1558	0.00	−5.5635	0.00	0.1169	0.00	−4.2335	0.00
Interface solid	0.1558	$4.47 \times 10^{-6}$	−5.5635	$1.49 \times 10^{-8}$	0.1169	$3.35 \times 10^{-4}$	−4.2335	$6.34 \times 10^{-5}$
Interface fluid	−0.1558	$4.47 \times 10^{-6}$	5.5635	$1.48 \times 10^{-8}$	−0.1169	$3.35 \times 10^{-4}$	4.2342	$1.78 \times 10^{-2}$
In–out	0.1558	$1.63 \times 10^{-3}$	5.5637	$3.20 \times 10^{-3}$	0.1169	$2.16 \times 10^{-3}$	4.2338	$8.12 \times 10^{-3}$

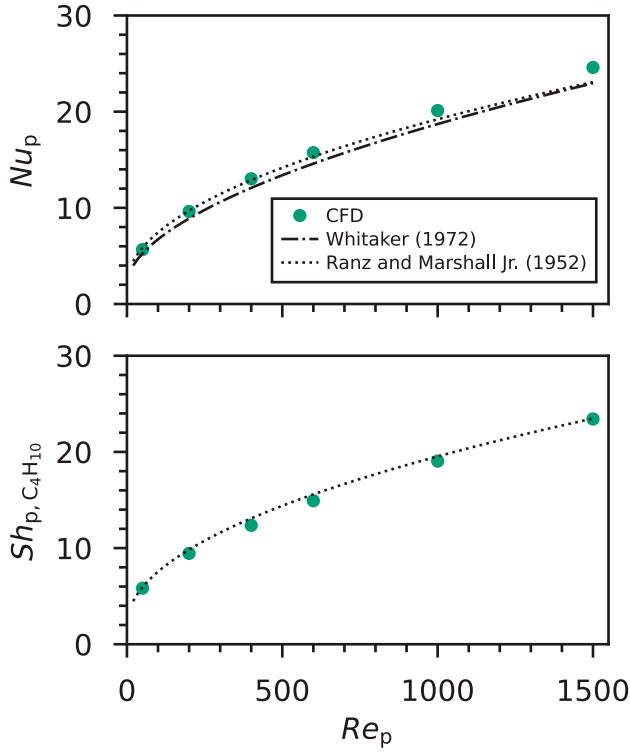


**Figure 8.** Comparison between the solid–fluid Nusselt and Sherwood numbers extracted from CFD and standard literature correlations.

the  $Sh_{p, C_4H_{10}}$  numbers are in excellent agreement with the correlations derived by Whitaker (1972) and Ranz and Marshall (1952a, 1952b), which is in line with the findings of Dixon et al. (2010). The literature correlations used are detailed in Section S7 of the supplemental data.

In addition to the particle Nusselt and Sherwood numbers, the 99% boundary layer thickness  $\delta_i$  of temperature ( $i = T$ ) and  $CO_2$  concentration ( $i = CO_2$ ) at the forward stagnation point are evaluated from the CFD simulations and compared with the definition of temperature and concentration boundary layer thickness according to Schlichting and Gersten (2017).

$$\delta_i = \delta_m X^{-1/3} \quad (31)$$

with the momentum boundary layer thickness  $\delta_m$  determined by Equation (26). The temperature boundary layer thickness  $\delta_T$  is calculated by inserting the Prandtl number  $Pr = c_{p,f} \mu_f / \lambda_f$  for  $X$ , and for the computation of the concentration boundary layer thickness  $\delta_{CO_2}$  the Schmidt number  $Sc_{CO_2} = \mu_f / \rho_f D_{m, CO_2}$  is used instead. The temperature and concentration boundary layer thickness becomes smaller with increasing  $Re_p$  and grows with decreasing Prandtl or Schmidt number, as shown in Figure 9. The CFD simulations agree well with the predictions of the equations presented by Schlichting and Gersten (2017).

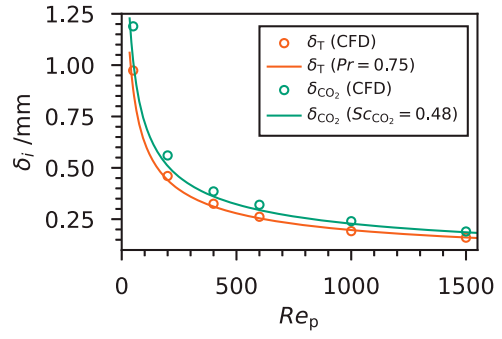


**Figure 9.** Temperature and  $CO_2$  concentration boundary layer thickness  $\delta_i$  at the forward stagnation point of a sphere determined from CFD simulations and calculated according to Schlichting and Gersten (2017) over particle Reynolds number  $Re_p$ .

This investigation demonstrates that coupling the fluid flow around a spherical VPO catalyst with the reaction inside a porous particle via the implemented conjugated heat and mass transfer model results in an accurate description of the transport at the interface. This is supported by comparisons with correlations and models in the relevant literature.

### 5.3. Packed bed of rings: impact of secondary gradient

The highest number of non-orthogonal cells, and consequently the largest effect of the secondary gradient on the simulation results, is expected for unstructured meshes of complex geometries. Therefore, the influence of the secondary gradient on integral and distributed quantities is investigated for the flow through a short packed bed containing ring shaped VPO catalyst particles. The simulation setup described in Section 4.3 is calculated once with consideration of the secondary gradient and once without it ( $\hat{S}_\kappa = 0$ ).

The quotient  $\hat{\mathbf{A}} \cdot \hat{\mathbf{A}} / \hat{\mathbf{A}} \cdot \hat{\mathbf{e}}_b$  can be used to quantify the level of non-orthogonality of an interface-nearest computational cell. The closer this quotient is to unity, the more similar the cell is to a perfectly orthogonal cell. Figure 10 shows the probability distribution of  $\hat{\mathbf{A}} \cdot \hat{\mathbf{A}} / \hat{\mathbf{A}} \cdot \hat{\mathbf{e}}_b$  for the interface-nearest cells and illustrates that a large percentage of the interface-nearest cells on the fluid and solid sides can be assumed to be approximately orthogonal. However, especially at the fluid side, there are a few cells that significantly deviate from orthogonality.

Table 3 lists various integral quantities characteristic of catalyst performance and heat removal obtained from simulations with and without a secondary gradient. The values calculated neglecting the secondary gradient differ only slightly from the values computed considering the secondary gradient. This indicates that applying the secondary gradient has a minor impact on the

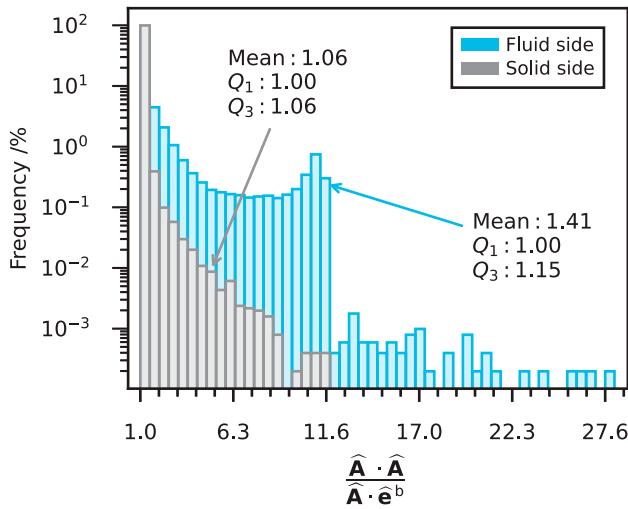


**Figure 10.** Probability distribution of  $\hat{\mathbf{A}} \cdot \hat{\mathbf{A}} / \hat{\mathbf{A}} \cdot \hat{\mathbf{e}}^b$  at the fluid and solid sides of the particle surface of a catalytic fixed bed.

**Table 3.** Integral quantities of the catalytic fixed bed simulated with and without considering the secondary gradient, and their relative deviation from each other.

Quantity	With secondary gradient	Without secondary gradient	Deviation (%)
$\chi_{C_4H_{10}}$ (%)	5.565	5.567	0.034
$S_{MA}$ (%)	70.344	70.346	0.002
$S_{CO}$ (%)	17.303	17.303	0.002
$S_{CO_2}$ (%)	12.353	12.351	0.014
$Q_{reaction}$ (W)	13.785	13.790	0.033
$Q_{removed}$ (W)	8.871	8.874	0.031
$\bar{T}_{surf}$ (K)	696.737	696.745	0.001
$T_{f,max}$ (K)	728.034	728.058	0.003
$T_{f,min}$ (K)	728.381	728.404	0.003

integral results of the simulation even for calculations with complex geometries. The small effect of the secondary gradient on integral quantities can be attributed to the high percentage of approximately orthogonal cells shown in Figure 10. This is in line with the finding of

Demirdžić and Muzaferija (1995), who concluded that the secondary gradient can be neglected for cells close to orthogonality.

To study the impact of the secondary gradient on distributed quantities, the deviation between the simulation with and without secondary gradient for the temperature and the mass fraction of  $n$ -butane at the fluid–solid interface is calculated and shown in Figure 11. Owing to the large number of approximately orthogonal cells, the difference between the simulations with and without secondary gradient is negligible for most of the temperatures and  $C_4H_{10}$  mass fractions at the interface. Nevertheless, there are regions on the particle surface at which the non-orthogonality of the interface-nearest cells results in deviations between simulation with and without secondary gradient by up to 0.5% in the temperature and by up to 8.2% in the  $C_4H_{10}$  mass fraction. As illustrated in Section S8 of the supplemental data, these regions are frequently located around particle–particle and particle–wall contacts, where the close proximity between surfaces results in non-orthogonal computational cells. In these regions, the high value of the quotient  $\hat{\mathbf{A}} \cdot \hat{\mathbf{A}} / \hat{\mathbf{A}} \cdot \hat{\mathbf{e}}^b$  results in an increase of the secondary gradient term (see Equation 21) and consequently its value becomes more important for the calculation of the scalar or scalar flux value at the fluid–solid interface. This demonstrates that neglecting the secondary gradient can have a significant effect locally on the temperatures and mass fractions at the particle surface.

Not applying secondary gradients in the conjugated heat and mass transfer model results in similar integral quantities as considering the secondary gradient, but may cause local deviations in the temperature and mass fractions distribution. For computational meshes with a higher amount of strongly non-orthogonal cells at the particle surface, it can be assumed that the local influence

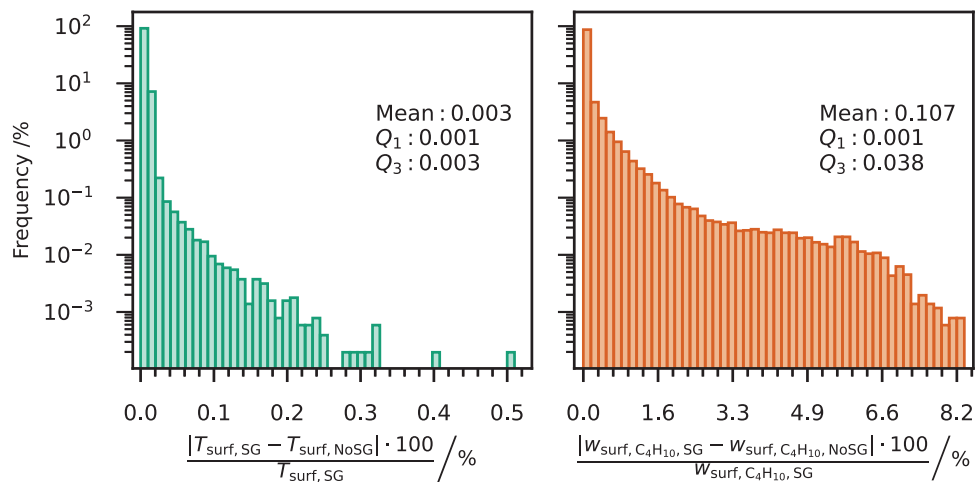


**Figure 11.** Probability distribution of the relative particle surface temperature (left) and  $C_4H_{10}$  mass fraction (right) deviation between a catalytic fixed bed calculated with (SG) and without (NoSG) a secondary gradient.

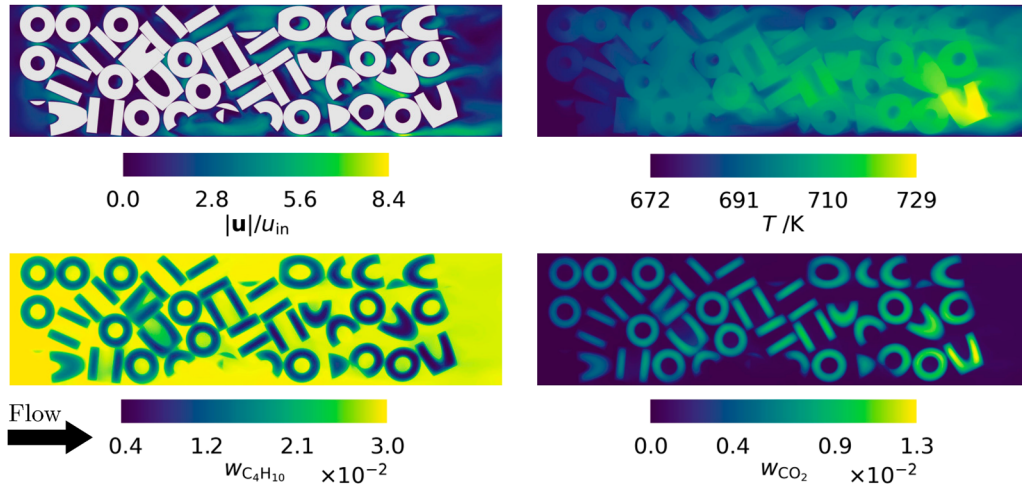


**Figure 12.** Normalized velocity magnitude (top left), temperature (top right),  $C_4H_{10}$  (bottom left), and  $CO_2$  (bottom right) mass fractions at a plane through the packed bed centre.

of the secondary gradient also affects integral quantities. Both simulations, with and without secondary gradient, reach convergence after 10,000 iteration steps. The CPU time per iteration of the simulation neglecting the secondary gradient is 252.67 s, while for the simulation considering the secondary gradient this value increases slightly to 252.85 s. Since significant differences in computational time and numerical stability between the simulation with and without secondary gradient cannot be found, it is recommended to consider the secondary gradient in the CHT and CMT model. Therefore, all further results presented in this study are based on simulation with a secondary gradient.

#### 5.4. Packed bed of rings: detailed analysis of catalyst performance

The performance of a catalyst used in a fixed bed is not only affected by its chemistry but also by transport processes within the fluid and solid phases and between both phases. Therefore, PRCFD simulations with reaction can help to gain a better understanding of the catalyst performance inside the reactor tube.

Figure 12 shows the normalized velocity magnitudes, temperatures, and  $n$ -butane and  $CO_2$  mass fractions at a plane containing the packed bed centre axis. The flow direction is from left to right with a particle Reynolds number of 200, i.e. in the laminar flow regime. The velocity is non-uniformly distributed over the tube length-section, indicating a strong deviation from plug-flow behaviour. The concentration of  $C_4H_{10}$  is reduced in axial direction by the reaction, whereas  $CO_2$  is formed from  $C_4H_{10}$  and MA. Similar to the observations made for the flow around a single VPO particle described in Section 5.2 and in line with the results of Partopour

and Dixon (2018) for a fixed bed containing spherical catalysts, the mass fraction gradients inside the particles are steep owing to the limitation by pore diffusion. However, a gradient of the  $n$ -butane and  $CO_2$  mass fraction towards the tube wall cannot be found—different from the study of Partopour and Dixon (2018) because in the present work a shorter fixed bed with a smaller tube-to-particle diameter-ratio ( $D_t/d_{p,outer} = 3.75$ ) is investigated. Owing to the exothermic reaction, the temperature increases along the packed bed length and decreases towards the cooling tube wall. As already reported by Dong et al. (2018), local temperature differences exceeding 40 K are observable within a single particle close to the tube wall. Moreover, the local packed bed structure and flow regime can lead to reduced heat transport in some regions of the packed bed, resulting in overheating of individual particles. The  $C_4H_{10}$  consumption significantly grows in these regions. In addition, and as also pointed out by Partopour and Dixon (2018), the  $CO_2$  mass fraction increases, since total oxidation is favoured by the high temperatures.

For a quantitative evaluation of the catalyst performance, the catalyst effectiveness factor  $\eta_{C_4H_{10},MA}$  of the reaction from  $C_4H_{10}$  to MA is calculated for every individual particle in the fixed bed. The catalyst effectiveness factor is the ratio of the volume averaged reaction rate over the entire particle to the area averaged reaction rate at the catalyst surface:

$$\eta_{C_4H_{10},MA} = \frac{\frac{1}{V_p} \int_V r_{C_4H_{10},MA} dV}{\frac{1}{A_p} \int_A r_{C_4H_{10},MA} dA} \quad (32)$$

The spatial distribution over the fixed bed and the axial profile of  $\eta_{C_4H_{10},MA}$  are illustrated in Figure 13. Owing to the temperature rise and the reduction of the reactant

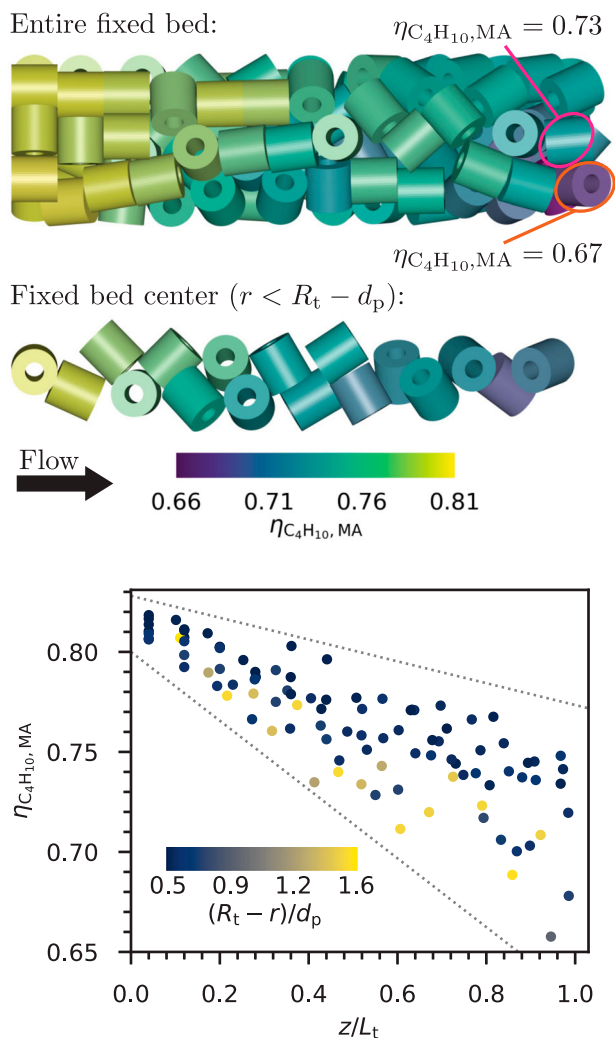


**Figure 13.** Spatial distribution (top) and axial profile (bottom) of the effectiveness factor for the reaction of  $C_4H_{10}$  to maleic anhydride. The colour of the dots represents the radial position  $(R_t - r)/d_p$ . The dotted lines are for orientation only.

*n*-butane, the effectiveness factor decreases along the packed bed length from 0.82 to 0.65. The cooling by the tube wall yields a higher  $\eta_{C_4H_{10},MA}$  for wall-near particles (indicated by darker colours). Nevertheless, the impact of the local packed bed structure and flow regime on the local transport phenomena and consequently on the local reactions leads to differences in the effectiveness factors of particles located on similar axial and radial positions. Moreover,  $\eta_{C_4H_{10},MA}$  of neighbouring particles can also differ significantly. Because of the increasing radial temperature gradients, the distribution of the effectiveness factor for particles with similar axial position becomes wider towards the end of the fixed bed. Reactors with longer fixed beds need to be simulated to verify if the width of this distribution declines after its maximum in the hot spot region.

## 6. Conclusion

In the work presented, a physically accurate and numerically stable conjugated heat and mass transfer model is proposed for coupling a catalytic reaction inside a porous catalyst particle with the surrounding fluid flow. Since the CHT and CMT model can be applied to computational meshes with orthogonal and non-orthogonal cells, the approach enables the simulation of even very complex geometries, such as packed beds of non-spherical pellets, that can only be solved with computational efficiency using unstructured meshes.

Regardless of whether the underlying mesh is structured or unstructured, the model implemented is able to reflect the analytical solution of heat and species mass diffusion through two connected slabs. Moreover, the particle Nusselt and Sherwood numbers, as well as the thickness of the temperature and concentration boundary layers at the forward stagnation point, are determined from the CFD simulation of the flow around a single spherical VPO particle coupled with reaction inside the porous catalyst. The values determined are in excellent agreement with results obtained from relevant literature correlations. In addition to the validation of the CHT and CMT model with analytical solutions and correlations, the impact of a secondary gradient on integral and distributed quantities is investigated for the flow through a short fixed bed containing ring-shaped VPO catalysts, as an illustrative example for a complex geometry resolved by an unstructured mesh. It can be seen that the secondary gradient does not have a significant influence on integral quantities but might affect the temperature and mass fractions locally at the fluid–solid interface. Furthermore, considering the secondary gradient does not change the numerical stability and computational effort of the simulation. Therefore, it is advisable to apply a secondary gradient, especially for unstructured meshes of complex geometry.

The approach presented for coupling the surrounding flow with reaction inside the porous catalyst is applied as an example on a short packed bed for maleic anhydride synthesis to obtain better insights into catalyst performance. The analysis of temperatures and mass fractions at a plane containing the packed bed centre axis indicates that individual particles overheat leading to an increase in  $CO_2$  mass fraction owing to the more favoured total oxidation of *n*-butane and MA. Moreover, the catalyst effectiveness factor of the reaction from  $C_4H_{10}$  to MA, being calculated for every single particle, is reduced in the axial direction and grows towards the tube wall. However, the effectiveness factor can differ for particles with similar axial and radial positions owing to the influence of the

local packed bed structure and flow regime on energy and material transport.

The method presented is a basis for the automated computer-aided shape optimization of catalyst particles. In addition to the PRCFD simulation of catalytic fixed beds, the conjugated heat and mass transfer model can also be applied in modelling other applications in which fluid flow must be coupled with transport inside a porous solid phase, such as monolithic catalysts (Boger et al., 2004), membrane filtration (Belfort, 1989), redox-flow batteries (Prumbohm et al., 2021), or fuel cells (Zhang & Jiao, 2018). In order to apply the CHT model to high-temperature processes, the influence of thermal radiation on the heat transfer should be considered. For a more detailed description of the species mass diffusion within multicomponent mixtures, future work should replace the Fickian approach with Maxwell–Stefan type models, as described for the fluid phase by Krishna and Wesselingh (1997) and for diffusion in porous catalyst particles by Donaubaue and Hinrichsen (2019). Finally, the comparison of the simulated results with spatially resolved measurements of temperature and gas composition in chemical reactors is crucial for further validation of the method.

## Nomenclature

### Latin symbols

$\hat{\mathbf{A}}$	boundary face normal
$A_p$	particle surface area ( $\text{m}^2$ )
$c_p$	specific heat capacity ( $\text{J kg}^{-1} \text{K}^{-1}$ )
$\mathbf{D}$	deformation tensor (Pa)
$D_{\text{eff},i}$	effective diffusion coefficient of component $i$ ( $\text{m}^2 \text{s}^{-1}$ )
$D_i$	diffusion coefficient of component $i$ ( $\text{m}^2 \text{s}^{-1}$ )
$D_{i,j}$	binary diffusion coefficient between component $i$ and $j$ ( $\text{m}^2 \text{s}^{-1}$ )
$D_{\text{Kn},i}$	Knudsen diffusion coefficient of component $i$ ( $\text{m}^2 \text{s}^{-1}$ )
$D_{\text{m},i}$	molecular diffusion coefficient of component $i$ ( $\text{m}^2 \text{s}^{-1}$ )
$D_t$	tube diameter (m)
$D_{\text{turb}}$	turbulent eddy diffusion coefficient ( $\text{m}^2 \text{s}^{-1}$ )
$d_b$	length of the vector between the cell centroid and the boundary face centroid (m)
$d_p$	particle diameter (m)
$d_{\text{p,inner}}$	hollow cylinder inner diameter (m)
$d_{\text{p,outer}}$	hollow cylinder outer diameter (m)
$\hat{\mathbf{e}}_b$	normalized vector between cell centroid and boundary face centroid
$\Delta H_{\text{react},j}^\circ$	specific standard enthalpy of reaction $j$ ( $\text{J kmol}^{-1}$ )

$h_i$	partial enthalpy of component $i$ ( $\text{J kg}^{-1}$ )
$h_p$	hollow cylinder height (m)
$h_{\text{tot}}$	total enthalpy ( $\text{J kg}^{-1}$ )
$\mathbf{I}$	identity tensor ( $\text{s}^{-1}$ )
$L_{\text{slab}}$	length of the slab (m)
$L_t$	packed bed length (m)
$\dot{M}_i$	species mass flow of component $i$ ( $\text{kg s}^{-1}$ )
$M_w$	molecular weight of the mixture ( $\text{kg kmol}^{-1}$ )
$M_{w,i}$	molecular weight of the component $i$ ( $\text{kg kmol}^{-1}$ )
$\mathbf{m}_i$	species mass flux vector of component $i$ ( $\text{kg m}^{-2} \text{s}^{-1}$ )
$N$	number of components
$N_{\text{react}}$	number of reactions
$p$	pressure (Pa)
$Q$	heat flow (W)
$Q_1$	first quartile
$Q_3$	third quartile
$\dot{Q}_{\text{reaction}}$	heat of reaction (W)
$\dot{Q}_{\text{removed}}$	removed heat (W)
$\mathfrak{R}$	ideal gas constant: $8314 \text{ J K}^{-1} \text{ kmol}^{-1}$
$R_t$	tube radius (m)
$r$	radial position (m)
$r_{\text{cat}}$	mean pore radius of the catalyst (m)
$r_j$	rate of reaction $j$ ( $\text{kmol s}^{-1} \text{ kg}_{\text{cat}}^{-1}$ )
$S$	constant volumetric heat source ( $\text{W m}^{-3}$ )
$S_i$	selectivity to component $i$ (%)
$\hat{S}_\kappa$	secondary gradient
$\mathbf{T}$	viscous stress tensor (Pa)
$\mathbf{T}_{\text{RANS}}$	Reynolds-averaged Navier–Stokes stress tensor (Pa)
$T$	temperature (K)
$T^+$	dimensionless temperature
$T_{f,\text{max}}$	maximum temperature of the fluid (K)
$T_{f,\text{min}}$	minimum temperature of the fluid (K)
$\bar{T}_{\text{surf}}$	average surface temperature (K)
$\mathbf{u}$	velocity vector ( $\text{m s}^{-1}$ )
$u^*$	velocity scale ( $\text{m s}^{-1}$ )
$V_p$	particle volume ( $\text{m}^3$ )
$w_i$	mass fraction of component $i$
$w_i^+$	dimensionless mass fraction of component $i$
$X_i$	conversion of component $i$ (%)
$x_i$	molar fraction of component $i$
$y^+$	dimensionless wall distance
$z$	axial position (mm)

### Greek symbols

$\Gamma$	transport parameter
$\delta_i$	concentration boundary layer thickness of component $i$ (m)
$\delta_{\text{m}}$	momentum boundary layer thickness (m)
$\delta_{\text{T}}$	temperature boundary layer thickness (m)

$\epsilon_{\text{cat}}$	catalyst porosity
$\zeta$	boundary condition
$\eta_j$	catalyst effectiveness factor of reaction $j$
$\kappa$	transfer coefficient
$\lambda$	thermal conductivity ( $\text{W m}^{-1} \text{K}^{-1}$ )
$\lambda_{\text{turb}}$	turbulent eddy thermal conductivity ( $\text{W m}^{-1} \text{K}^{-1}$ )
$\mu$	dynamic viscosity (Pa s)
$\mu_{\text{turb}}$	turbulent eddy viscosity (Pa s)
$\nu_{i,j}$	stoichiometric coefficient of component $i$ in reaction $j$
$\rho$	density ( $\text{kg m}^{-3}$ )
$\tau$	under-relaxation factor
$\tau_{\text{cat}}$	catalyst tortuosity
$\phi$	scalar value
$\phi^+$	dimensionless scalar value
$\dot{\omega}$	scalar flux

### Dimensionless numbers

$Nu_p$	particle Nusselt number $Nu_p = h d_p / \lambda_f$
$Pr$	Prandtl number: $Pr = c_{p,f} \mu_f / \lambda_f$
$Pr_{\text{turb}}$	turbulent Prandtl number: $Pr_{\text{turb}} = c_{p,f} \mu_{\text{turb}} / \lambda_{\text{turb}}$
$Re_p$	particle Reynolds number: $Re_p = u_{\text{in}} \rho_f d_p / \mu_f$
$Sc_i$	Schmidt number of component $i$ : $Sc_i = \mu_f / D_{m,i} \rho_f$
$Sc_{\text{turb}}$	turbulent Schmidt number: $Sc_{\text{turb}} = \mu_{\text{turb}} / D_{\text{turb}} \rho_f$
$Sh_{p,i}$	particle Sherwood number of component $i$ : $Sh_{p,i} = k_i d_p / D_{m,i}$

### Subscripts

ax	axial
b	boundary
c	centroid
eff	effective
f	fluid
in	inlet
lam	laminar
NoSG	without secondary gradient
SG	with secondary gradient
s	solid
surf	particle surface
turb	turbulent
wall	tube wall

### Abbreviations

CFD	Computational Fluid Dynamics
CHT	Conjugated Heat Transfer
CMT	Conjugated Mass Transfer

IUU	Iterations Until Update
MA	Maleic Anhydride
PRCFD	Particle-Resolved Computational Fluid Dynamics
RANS	Reynolds-Averaged Navier-Stokes
VPO	Vanadium Phosphorus Oxide

### Data deposition

Supplemental material with figure data, a STL file of the simulated fixed bed geometry, and the spatial distribution of the effectiveness factor as Blender file is available under: <https://zenodo.org/doi/10.5281/zenodo.8195971>.

### Note

The preprint of this article is available at <https://chemrxiv.org/engage/chemrxiv/article-details/64c58e1ace23211b20c8414a>

### Acknowledgements

The authors thank the Simulation Science Center Clausthal and Göttingen (SWZ) for providing high performance computing facilities.

### Disclosure statement

The authors report there are no competing interests to declare.

### Funding

The authors acknowledge financial support from the Open Access Publishing Fund of Clausthal University of Technology.

### References

- Belfort, G. (1989). Fluid mechanics in membrane filtration: Recent developments. *Journal of Membrane Science*, 40(2), 123–147. [https://doi.org/10.1016/0376-7388\(89\)89001-5](https://doi.org/10.1016/0376-7388(89)89001-5)
- Boger, T., Heibel, A. K., & Sorensen, C. M. (2004). Monolithic catalysts for the chemical industry. *Industrial & Engineering Chemistry Research*, 43(16), 4602–4611. <https://doi.org/10.1021/ie030730q>
- Bosanquet, C. H. (1944). *The optimum pressure for a diffusion separation plant*. British TA Report BR-507, September 27.
- Clift, R., Grace, J. R., & Weber, M. E. (2013). *Bubbles, drops, and particles*. Dover.
- Demirdžić, I., & Muzaferija, S. (1995). Numerical method for coupled fluid flow, heat transfer and stress analysis using unstructured moving meshes with cells of arbitrary topology. *Computer Methods in Applied Mechanics and Engineering*, 125(1-4), 235–255. [https://doi.org/10.1016/0045-7825\(95\)00800-G](https://doi.org/10.1016/0045-7825(95)00800-G)
- Dhole, S. D., Chhabra, R. P., & Eswaran, V. (2006). A numerical study on the forced convection heat transfer from an isothermal and isoflux sphere in the steady symmetric flow regime. *International Journal of Heat and Mass Transfer*, 49(5-6), 984–994. <https://doi.org/10.1016/j.ijheatmasstransfer.2005.09.010>
- Dixon, A. G. (2021a). Local structure effects on heat transfer in very low tube-to-particle diameter ratio fixed beds

- of spheres. *Industrial & Engineering Chemistry Research*, 60(27), 9777–9786. <https://doi.org/10.1021/acs.iecr.1c01660>
- Dixon, A. G. (2021b). Local transport and reaction rates in a fixed bed reactor tube: Exothermic partial oxidation of ethylene. *Chemical Engineering Science*, 231, 116305. <https://doi.org/10.1016/j.ces.2020.116305>
- Dixon, A. G., Nijemeisland, M., & Stitt, E. H. (2005). CFD study of heat transfer near and at the wall of a fixed bed reactor tube: Effect of wall conduction. *Industrial & Engineering Chemistry Research*, 44(16), 6342–6353. <https://doi.org/10.1021/ie049183e>
- Dixon, A. G., & Partopour, B. (2020). Computational fluid dynamics for fixed bed reactor design. *Annual Review of Chemical and Biomolecular Engineering*, 11, 109–130. <https://doi.org/10.1146/chembioeng.2020.11.issue-1>
- Dixon, A. G., Taskin, M. E., Nijemeisland, M., & Stitt, E. H. (2010). CFD method to couple three-dimensional transport and reaction inside catalyst particles to the fixed bed flow field. *Industrial & Engineering Chemistry Research*, 49(19), 9012–9025. <https://doi.org/10.1021/ie100298q>
- Dixon, A. G., Taskin, M. E., Nijemeisland, M., & Stitt, E. H. (2011). Systematic mesh development for 3D CFD simulation of fixed beds: Single sphere study. *Computers & Chemical Engineering*, 35(7), 1171–1185. <https://doi.org/10.1016/j.compchemeng.2010.12.006>
- Donaubauer, P. J., & Hinrichsen, O. (2019). Evaluation of effectiveness factors for multicomponent diffusion models inside 3D catalyst shapes. *Industrial & Engineering Chemistry Research*, 58(1), 110–119. <https://doi.org/10.1021/acs.iecr.8b04922>
- Dong, Y., Geske, M., Korup, O., Ellenfeld, N., Rosowski, F., Dobner, C., & Horn, R. (2018). What happens in a catalytic fixed-bed reactor for *n*-butane oxidation to maleic anhydride? Insights from spatial profile measurements and particle resolved CFD simulations. *Chemical Engineering Journal*, 350, 799–811. <https://doi.org/10.1016/j.cej.2018.05.192>
- Eigenberger, G., & Ruppel, W. (2012). Catalytic fixed-bed reactors. In *Ullmann's encyclopedia of industrial chemistry* (pp. 1–66). Wiley-VCH Verlag.
- Ertl, G., Knözinger, H., & Weitkamp, J. (Eds.). (1997). *Handbook of heterogeneous catalysis*. Wiley-VCH Verlag.
- Fairbanks, D. F., & Wilke, C. R. (1950). Diffusion coefficients in multicomponent gas mixtures. *Industrial & Engineering Chemistry*, 42(3), 471–475. <https://doi.org/10.1021/ie50483a022>
- Flaischlen, S., Kutscherauer, M., & Wehinger, G. D. (2021). Local structure effects on pressure drop in slender fixed beds of spheres. *Chemie Ingenieur Technik*, 93(1–2), 273–281. <https://doi.org/10.1002/cite.v93.1-2>
- Flaischlen, S., & Wehinger, G. D. (2019). Synthetic packed-bed generation for CFD simulations: Blender vs. STAR-CCM+. *ChemEngineering*, 3(2), 52. <https://doi.org/10.3390/chemengineering3020052>
- Freund, H., Zeiser, T., Huber, F., Klemm, E., Brenner, G., Durst, F., & Emig, G. (2003). Numerical simulations of single phase reacting flows in randomly packed fixed-bed reactors and experimental validation. *Chemical Engineering Science*, 58(3), 903–910. [https://doi.org/10.1016/S0009-2509\(02\)00622-X](https://doi.org/10.1016/S0009-2509(02)00622-X)
- Fuller, E. N., Schettler, P. D., & Giddings, J. C. (1966). New method for prediction of binary gas-phase diffusion coefficients. *Industrial & Engineering Chemistry*, 58(5), 18–27. <https://doi.org/10.1021/ie50677a007>
- Jakobsen, H. A. (2014). *Chemical reactor modeling multiphase reactive flows*. Springer International.
- Jurtz, N., Flaischlen, S., Scherf, S. C., Kraume, M., & Wehinger, G. D. (2020). Enhancing the thermal performance of slender packed beds through internal heat fins. *Processes*, 8(12), 1528. <https://doi.org/10.3390/pr8121528>
- Jurtz, N., Kraume, M., & Wehinger, G. D. (2019). Advances in fixed-bed reactor modeling using particle-resolved computational fluid dynamics (CFD). *Reviews in Chemical Engineering*, 35(2), 139–190. <https://doi.org/10.1515/revce-2017-0059>
- Jurtz, N., Waldherr, P., & Kraume, M. (2019). Numerical analysis of the impact of particle friction on bed voidage in fixed-beds. *Chemie Ingenieur Technik*, 91(9), 1260–1266. <https://doi.org/10.1002/cite.v91.9>
- Kader, B. A. (1981). Temperature and concentration profiles in fully turbulent boundary layers. *International Journal of Heat and Mass Transfer*, 24(9), 1541–1544. [https://doi.org/10.1016/0017-9310\(81\)90220-9](https://doi.org/10.1016/0017-9310(81)90220-9)
- Kee, R. J., Dixon-Lewis, G., Warnatz, J., Coltrin, M. E., & Miller, J. A. (1986). *A Fortran computer code package for the evaluation of gas-phase multicomponent transport properties*. Sandia National Laboratories Report SAND-86-8246. <https://www.osti.gov/biblio/7157265>
- Kolaczkowski, S. T., Chao, R., Awdry, S., & Smith, A. (2007). Application of a CFD code (FLUENT) to formulate models of catalytic gas phase reactions in porous catalyst pellets. *Chemical Engineering Research and Design*, 85(11), 1539–1552. <https://doi.org/10.1205/cherd06226>
- Krishna, R., & Wesselingh, J. A. (1997). The Maxwell–Stefan approach to mass transfer. *Chemical Engineering Science*, 52(6), 861–911. [https://doi.org/10.1016/S0009-2509\(96\)00458-7](https://doi.org/10.1016/S0009-2509(96)00458-7)
- Kutscherauer, M., Böcklein, S., Mestl, G., Turek, T., & Wehinger, G. D. (2022). An improved contact modification routine for a computationally efficient CFD simulation of packed beds. *Chemical Engineering Journal Advances*, 9, 100197. <https://doi.org/10.1016/j.cej.2021.100197>
- Kutscherauer, M., Reinold, P., Böcklein, S., Mestl, G., Turek, T., & Wehinger, G. D. (2023). How temperature measurement impacts pressure drop and heat transport in slender fixed beds of Raschig rings. *ACS Engineering Au*, 3(1), 45–58. <https://doi.org/10.1021/acengineeringau.2c00039>
- Lesser, D., Mestl, G., & Turek, T. (2016). Transient behavior of vanadyl pyrophosphate catalysts during the partial oxidation of *n*-butane in industrial-sized, fixed bed reactors. *Applied Catalysis A: General*, 510, 1–10. <https://doi.org/10.1016/j.apcata.2015.11.002>
- Lesser, D., Mestl, G., & Turek, T. (2017). Modeling the dynamic behavior of industrial fixed bed reactors for the manufacture of maleic anhydride. *Chemical Engineering Science*, 172, 559–570. <https://doi.org/10.1016/j.ces.2017.06.049>
- Maestri, M., & Cuoci, A. (2013). Coupling CFD with detailed microkinetic modeling in heterogeneous catalysis. *Chemical Engineering Science*, 96, 106–117. <https://doi.org/10.1016/j.ces.2013.03.048>
- Maffei, T., Gentile, G., Rebughini, S., Bracconi, M., Manelli, F., Lipp, S., Cuoci, A., & Maestri, M. (2016). A multi-region operator-splitting CFD approach for coupling microkinetic modeling with internal porous transport in heterogeneous catalytic reactors. *Chemical Engineering Journal*, 283, 1392–1404. <https://doi.org/10.1016/j.cej.2015.08.080>

- Mathur, S. R., & Murthy, J. Y. (1997). A pressure-based method for unstructured meshes. *Numerical Heat Transfer, Part B: Fundamentals*, 31(2), 195–215. <https://doi.org/10.1080/10407799708915105>
- Müller, M., Kutscherauer, M., Böcklein, S., Mestl, G., & Turek, T. (2021). Improved kinetics of *n*-butane oxidation to maleic anhydride: The role of byproducts. *Industrial & Engineering Chemistry Research*, 60(1), 218–229. <https://doi.org/10.1021/acs.iecr.0c05029>
- Müller, M., Kutscherauer, M., Böcklein, S., Wehinger, G. D., Turek, T., & Mestl, G. (2022). Modeling the selective oxidation of *n*-butane to maleic anhydride: From active site to industrial reactor. *Catalysis Today*, 387, 82–106. <https://doi.org/10.1016/j.cattod.2021.04.009>
- Murthy, J. Y., & Mathur, S. R. (1998). Computation of anisotropic conduction using unstructured meshes. *Journal of Heat Transfer*, 120(3), 583–591. <https://doi.org/10.1115/1.2824315>
- Partopour, B., & Dixon, A. G. (2017). An integrated workflow for resolved-particle packed bed models with complex particle shapes. *Powder Technology*, 322, 258–272. <https://doi.org/10.1016/j.powtec.2017.09.009>
- Partopour, B., & Dixon, A. G. (2018). *n*-Butane partial oxidation in a fixed bed: A resolved particle computational fluid dynamics simulation. *The Canadian Journal of Chemical Engineering*, 96(9), 1946–1956. <https://doi.org/10.1002/cjce.v96.9>
- Pasdunkorale, J., & Turner, I. W. (2003). A second order finite volume technique for simulating transport in anisotropic media. *International Journal of Numerical Methods for Heat & Fluid Flow*, 13(1), 31–56. <https://doi.org/10.1108/09615530310456750>
- Prumbohm, E., Becker, M., Flaischlen, S., Wehinger, G. D., & Turek, T. (2021). Flow field designs developed by comprehensive CFD model decrease system costs of vanadium redox-flow batteries. *Journal of Flow Chemistry*, 11(3), 461–481. <https://doi.org/10.1007/s41981-021-00165-2>
- Ranz, W. E., & Marshall, W. R., Jr. (1952a). Evaporation from drops (Part I). *Chemical Engineering Progress*, 48, 141–146.
- Ranz, W. E., & Marshall, W. R., Jr. (1952b). Evaporation from drops (Part II). *Chemical Engineering Progress*, 48, 173–180.
- Reichardt, H. (1951). Vollständige Darstellung der turbulenten Geschwindigkeitsverteilung in glatten Leitungen. *ZAMM – Journal of Applied Mathematics and Mechanics/Zeitschrift für Angewandte Mathematik und Mechanik*, 31(7), 208–219. <https://doi.org/10.1002/zamm.v31:7>
- Schlichting, H., & Gersten, K. (2017). *Boundary-Layer theory*. Springer.
- Shih, T.-H., Liou, W. W., Shabbir, A., Yang, Z., & Zhu, J. (1995). A new *k*- $\epsilon$  eddy viscosity model for high Reynolds number turbulent flows. *Computers & Fluids*, 24(3), 227–238. [https://doi.org/10.1016/0045-7930\(94\)00032-T](https://doi.org/10.1016/0045-7930(94)00032-T)
- Wehinger, G. D., Ambrosetti, M., Cheula, R., Ding, Z.-B., Isov, M., Kreitz, B., Kuhlmann, K., Kutscherauer, M., Niyogi, K., Poissonnier, J., Réocreux, R., Rudolf, D., Wagner, J., Zimmermann, R., Bracconi, M., Freund, H., Krewer, U., & Maestri, M. (2022). Quo vadis multi-scale modeling in reaction engineering? – A perspective. *Chemical Engineering Research and Design*, 184, 39–58. <https://doi.org/10.1016/j.cherd.2022.05.030>
- Wehinger, G. D., Eppinger, T., & Kraume, M. (2015). Evaluating catalytic fixed-bed reactors for dry reforming of methane with detailed CFD. *Chemie Ingenieur Technik*, 87(6), 734–745. <https://doi.org/10.1002/cite.v87.6>
- Wehinger, G. D., Klippel, F., & Kraume, M. (2017). Modeling pore processes for particle-resolved CFD simulations of catalytic fixed-bed reactors. *Computers & Chemical Engineering*, 101, 11–22. <https://doi.org/10.1016/j.compchemeng.2017.02.029>
- Whitaker, S. (1972). Forced convection heat transfer correlations for flow in pipes, past flat plates, single cylinders, single spheres, and for flow in packed beds and tube bundles. *AIChE Journal*, 18(2), 361–371. <https://doi.org/10.1002/aic.v18:2>
- Zhang, G., & Jiao, K. (2018). Multi-phase models for water and thermal management of proton exchange membrane fuel cell: A review. *Journal of Power Sources*, 391, 120–133. <https://doi.org/10.1016/j.jpowsour.2018.04.071>
- Ziółkowska, I., & Ziółkowski, D. (1988). Fluid flow inside packed beds. *Chemical Engineering and Processing: Process Intensification*, 23(3), 137–164. [https://doi.org/10.1016/0255-2701\(88\)80012-6](https://doi.org/10.1016/0255-2701(88)80012-6)